

Thermally-activated coercivity in core-shell permanent magnets

S. Bance,^{1,a)} J. Fischbacher,¹⁾ and T. Schrefl^{1,2)}

¹ *Industrial Simulation, St Pölten University of Applied Sciences, A-3100 St Pölten, Austria*

² *Centre for Integrated Sensor Systems, Danube University Krems, A-2700 Wiener Neustadt, Austria*

Finite element micromagnetic simulations are used to compute the temperature-dependent hysteresis properties of Nd₂Fe₁₄B permanent magnets in order to assess the influence of a hard (Dy,Nd)₂Fe₁₄B shell. The simulations show that the 4 nm thick shell cancels out the reduction in coercivity from an outer defect layer, which is known to exist at the grain boundaries in NdFeB permanent magnets. Activation volumes are computed and shown to depend on the structure's configuration as well as the temperature.

I. INTRODUCTION

Permanent magnets are key components in many important modern technologies, for example in direct-drive wind power generators and the motors in electric and hybrid vehicles [1]. A large percentage of modern high performance permanent magnets are based on Nd₂Fe₁₄B. In many applications these magnets are used at elevated temperatures, for example the operating temperature of the motors inside hybrid vehicles is around 450 K. At increased temperatures the effects of thermal activation on the reversal process are increased, reducing the coercivity, so some of the neodymium (Nd) is replaced by heavy rare earth elements such as dysprosium (Dy). (Dy,Nd)₂Fe₁₄B has a higher intrinsic anisotropy field so magnets containing Dy have a larger coercive field when compared to Nd₂Fe₁₄B magnets. (Dy,Nd)₂Fe₁₄B-containing magnets may be prepared either by adding Dy to the main phase during the alloying step or by adding Dy in a way that the (Dy,Nd)₂Fe₁₄B forms only near the grain boundaries, creating a hard shell-like layer. Possible routes for the latter process are the adding of Dy₂O₃ as a sintering element [2], [3] or by grain boundary diffusion [4]. This follows recent trends in the fabrication of nanostructured permanent magnets where hard magnetic phases with high intrinsic coercivity are being coupled to softer magnetic phases that exhibit high intrinsic magnetization in order to create magnetic materials with high values of energy product $(BH)_{\max}$ [5]–[8].

Recent advances in fabrication, characterization and simulation have emphasized the importance of surface defects with reduced anisotropy to the measured coercivity of rare earth permanent magnets [9]–[11]. It is possible that the grain boundary diffusion process could be optimized to produce a shell with an ideal ratio of Dy to Nd and an ideal shell thickness so that the coercivity is enhanced without too much reduction in remanence, leading to the desired high values of energy product $(BH)_{\max}$.

a) Author to whom correspondence should be addressed. Electronic mail: s.g.bance@gmail.com. Web: <http://academic.bancey.com>

In this work finite element micromagnetic simulations are used to calculate the thermally-activated extrinsic properties of NdFeB grains containing Dy-diffused hard shells in order to measure the influence of the thermal reduction in coercivity, the reduction in coercivity from a soft outer defect layer and the hardening from the Dy.

II. METHOD

In the present work finite element micromagnetic simulations [12], [13] are applied to compute the temperature-dependent hysteresis properties of single-grain Nd₂Fe₁₄B permanent magnets, considering the influence of a soft outer defect and a hard shell.

A. Model

Dodecahedral grain models, approximating the polyhedral geometries of grains observed in actual rare earth permanent magnets, are prepared in three varieties: (i) a pure Nd₂Fe₁₄B grain with no defect and no shell, (ii) a Nd₂Fe₁₄B core with a soft outer defect of 2 nm thickness and (iii) a Nd₂Fe₁₄B core with a hard (Dy,Nd)₂Fe₁₄B shell of 4 nm and an outer defect (2nm). The outer grain diameter is constant at 50 nm (Figure 1).

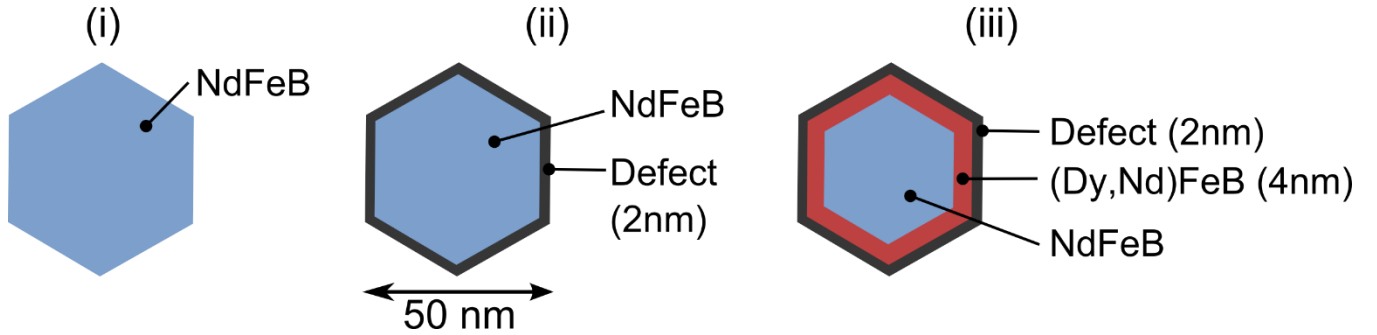


FIG. 1. Schematics of the three dodecahedral single grain models: (i) pure Nd₂Fe₁₄B, (ii) Nd₂Fe₁₄B core with a soft 2 nm thick outer defect layer, (iii) Nd₂Fe₁₄B core, 4 nm thick super-hard Dy-diffused layer and a 2 nm thick soft defect.

An adaptive mesh size is used in consideration of the critical lengths of the material, as suggested by Rave and co-workers (Figure 2) [14]. The theoretical exchange length of a ferromagnet is defined analytically as $L_d = \sqrt{A/K}$ where A is the exchange constant and K is the uniaxial magneto-crystalline anisotropy constant. At the outer corners of the model a mesh size of half the exchange length is assigned. At the outer edges a size corresponding to the domain wall width of $\delta = \pi L_d$ is assigned. The mesh edge length grows in size towards the center of the grain up to a maximum value of $5L_d$. The temperature-dependent material constants used in the simulations are given in Table I.

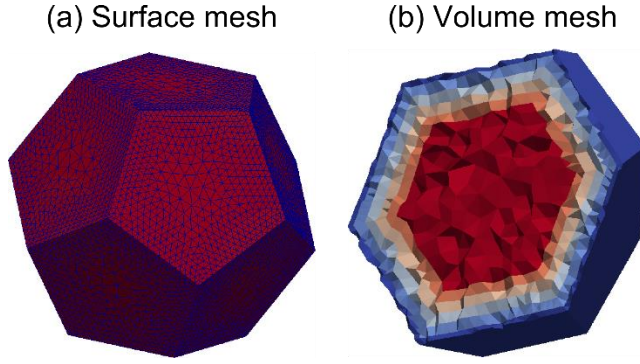


FIG. 2. Visualizations of the generated grain models showing (a) the surface mesh elements and (b) the inner volume elements. Additional shell layers were included to allow flexible reuse of the model, but were not used for the simulations contained within this article.

TABLE I. Intrinsic material properties used for the simulations. All values for $\text{Nd}_2\text{Fe}_{14}\text{B}$ from ref. [15]. Values of K and J_s for $(\text{Dy}_{47},\text{Nd}_{53})_2\text{Fe}_{14}\text{B}$ from ref. [16]. Values of A for $(\text{Dy}_{47},\text{Nd}_{53})_2\text{Fe}_{14}\text{B}$ from ref. [17].

Material	T [K]	K [MJ/m ³]	J_s [T]	A [pJ/m]
$\text{Nd}_2\text{Fe}_{14}\text{B}$	300	4.30	1.613	7.70
$\text{Nd}_2\text{Fe}_{14}\text{B}$	450	2.90	1.285	4.89
$(\text{Dy}_{47},\text{Nd}_{53})_2\text{Fe}_{14}\text{B}$	300	5.17	1.151	8.70
$(\text{Dy}_{47},\text{Nd}_{53})_2\text{Fe}_{14}\text{B}$	450	2.70	0.990	6.44

B. Simulation

The magnetization is interpolated piecewise linearly on a tetrahedral computational grid. The demagnetizing field $H_d = -\Delta U$ is computed from a magnetic scalar potential, U . In order to apply the boundary condition $U = 0$ at infinity, the finite element mesh is extended outside the magnetic particle. The parallelepipedic shell transformation [17] is applied in order to map the exterior mesh to the infinite exterior region. The demagnetization curve is computed by minimizing the micromagnetic energy for decreasing external field H with a field step of $\mu_0\Delta H = 0.01$ T. At each field the Landau-Lifshitz equation is integrated with infinite damping [18] using a semi-implicit midpoint-scheme [19] and a modified Barzilai-Borwein step length selection [20]. This algorithm [12] resembles a gradient descent method for energy minimization. With thermal activation the system can hop over a finite energy barrier which leads to a reduction in the switching field. Taking the intermediate magnetization configurations during reversal as an initial guess the modified string method [21] is used to find the minimum energy path and its associated energy barrier ΔE between the initial and reversed states. This is repeated as a function of applied field and the resulting energy barriers are fitted to an effective energy barrier function [22]

$$\Delta E = \Delta E_0(1 - H/H_{c,static})^n \quad (1)$$

using ΔE_0 and n as fitting parameters where ΔE_0 is the energy barrier for zero applied field, n is an unknown exponent and $H_{c,static}$ is the coercive field calculated from the static demagnetizing curve. This allows an approximation of the thermally-activated coercive field, which is the field corresponding to an energy barrier of $25k_B T$ [23]. The so-called phenomenological activation volume of reversal [26] can be approximated from the gradient at $25k_B T$ by Equation (2).

$$v = -\frac{1}{\mu_0 M_s} \frac{dE}{dH} \quad (2)$$

III. RESULTS & DISCUSSION

Figure 3 contains visualizations of the reversal process in the three models at 300 K. The reversal processes at 450 K are visually identical, albeit with slightly larger reversal domains. The theoretical anisotropy field $\mu_0 H_A = 2K_1/M_s$ equals 6.70 T for the pure $Nd_2Fe_{14}B$ grain at 300 K and 5.67 T at 450 K. The reduction in the calculated values can be attributed to the dodecahedral shape, which introduces a non-zero demagnetizing factor and edge effects, reducing the coercive field relative to H_A , which is based on a sphere. Reversal begins at an edge or corner of the grain, where locally non-uniform demagnetizing fields induce a perturbation in the magnetization.

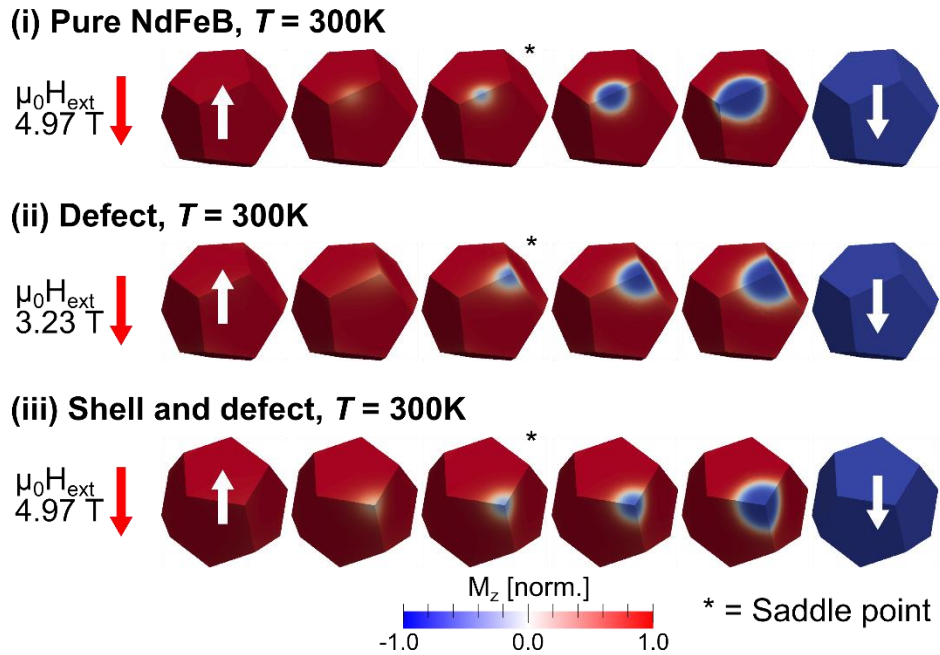


FIG. 3. Reversal processes in the single grain models with (i) a pure NdFeB grain, (ii) a NdFeB grain with a soft outer defect and (iii) NdFeB core, (Dy, Nd)FeB shell and an outer soft defect. Thermally-activated coercive field values are indicated with the field direction (red arrows). The saddle point image is the configuration with the highest total energy, forming the peak of the energy barrier.

Figures 4 and 5 contain the results of fitting the Energy barrier heights as a function of applied field to Equation (1) for $T = 300$ K and $T = 450$ K, respectively. The intersection of these fit lines by the $\Delta E = 25 k_B T$ line gives the estimated coercive field values for thermally-activated reversal. These thermally-activated coercive field values are given alongside the results of the static simulations in Table II. For the soft defect layer the material properties of the neighboring phase are used with the uniaxial anisotropy constant K adjusted to zero. In all three models, at $T = 300$ K the thermal activation reduces the coercivity by around 15%, while at 450 K the reduction is around 25%.

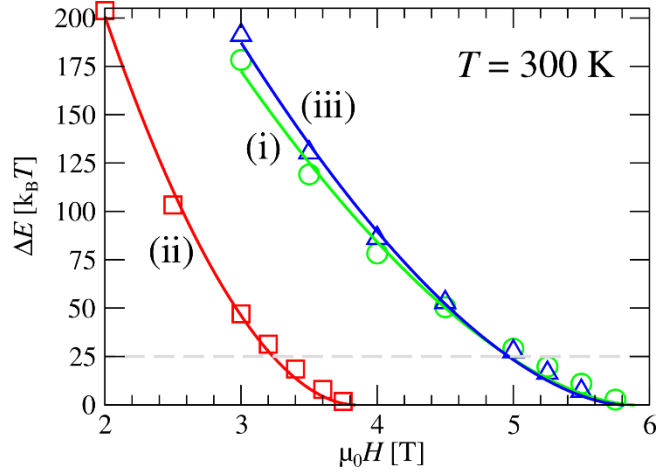


FIG. 4. Data and associated fits to Equation (1) of the energy barriers as a function of applied field strength at $T = 300$ K for (i) a single grain of $\text{Nd}_2\text{Fe}_{14}\text{B}$, (ii) a $\text{Nd}_2\text{Fe}_{14}\text{B}$ grain with a soft surface defect and (iii) a $\text{Nd}_2\text{Fe}_{14}\text{B}$ grain with a $(\text{Dy}_{47}, \text{Nd}_{53})_2\text{Fe}_{14}\text{B}$ shell and an outer surface defect. The dashed line indicates the $25 k_B T$ energy barrier height corresponding to thermally-activated coercivity.

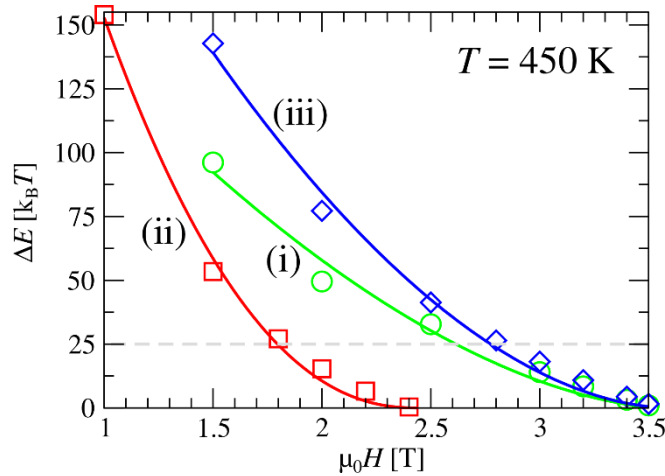


FIG. 5. Data and associated fits to Equation (1) of the energy barriers as a function of applied field strength at $T = 450$ K for (i) a single grain of $\text{Nd}_2\text{Fe}_{14}\text{B}$, (ii) a $\text{Nd}_2\text{Fe}_{14}\text{B}$ grain with a soft surface defect and (iii) a $\text{Nd}_2\text{Fe}_{14}\text{B}$ grain with a $(\text{Dy}_{47}, \text{Nd}_{53})_2\text{Fe}_{14}\text{B}$ shell and an outer surface defect. The dashed line indicates the $25 k_B T$ energy barrier height corresponding to thermally-activated coercivity.

At both temperatures the reduction in coercivity from the soft defect in (ii) is canceled out by the hard shell in (iii). At 300 K the thermally-activated coercive field for both (i) and (iii) are 4.97 T, whereas with a defect and no shell it is 3.23 T. At 450 K the equivalent values are (i) 2.62 T, (ii) 1.80 T and (iii) 2.78 T.

TABLE II. Results: static and thermally-activated coercivities and the reduction percentage caused by thermal activation for each model and both temperatures.

Model	T [K]	Static μ_0H_c [T]	Thermal μ_0H_c [T]	Reduction %
(i)	300	5.89	4.97	15.6
(i)	450	3.58	2.62	27.0
(ii)	300	3.84	3.23	15.8
(ii)	450	2.44	1.80	26.4
(iii)	300	5.81	4.97	14.5
(iii)	450	3.60	2.78	22.9

The activation volumes for all three models and both temperatures are calculated using the gradient of each fit at $25 k_B T$ and given in Table III. Activation volumes are greater in size at the higher temperature. The inclusion of the soft outer defect in model (ii) increases the phenomenological activation volume to around double the size in model (i) since the activation volume is proportional to the change in magnetization, which is larger when the reversal domain is located inside a soft magnetic phase. Likewise, the inclusion of the hard shell in model (iii) reduces the activation volume size back down by around one third.

TABLE III. Activation volumes of models (i), (ii) and (iii) measured at $T = 300$ K and $T = 450$ K using the gradient method of Gaunt & Roy [26].

Model	T [K]	v [nm^3]
(i)	300	148.0
(i)	450	267.3
(ii)	300	249.7
(ii)	450	530.8
(iii)	300	176.1
(iii)	450	365.0

IV. CONCLUSIONS

A $(\text{Dy}_{47}, \text{Nd}_{53})_2\text{Fe}_{14}\text{B}$ shell of 4 nm cancels out the reduction of coercivity from 2 nm thick soft surface defects. In addition to the decrease of the anisotropy field with temperature, thermal fluctuations cause a reduction of the coercive field. At $T = 300\text{K}$ thermal activation reduces the coercivity by 15%, while at 450 K the reduction is around 25%. The soft surface defect doubles the size of the activation volume, whereas the hard $(\text{Dy}_{47}, \text{Nd}_{53})_2\text{Fe}_{14}\text{B}$ shell reduces it by around one third.

ACKNOWLEDGMENTS

The authors would like to acknowledge funding support from the Replacement and Original Magnet Engineering Options (ROME) Seventh Framework Program (FP7).

REFERENCES

- [1] O. Gutfleisch, M. A. Willard, E. Brück, C. H. Chen, S. G. Sankar, and J. P. Liu, “Magnetic Materials and Devices for the 21st Century: Stronger, Lighter, and More Energy Efficient,” *Adv. Mater.*, vol. 23, no. 7, pp. 821–842, Feb. 2011.
- [2] M. H. Ghandehari and J. Fidler, “Microstructural Studies of High Coercivity Nd₁₅Fe₇₇B₈ Sintered Magnets,” in *MRS Proceedings*, 1987, vol. 96, p. 193.
- [3] M. H. Ghandehari and J. Fidler, “Microstructural evidence for the magnetic surface hardening of Dy₂O₃-doped Nd₁₅Fe₇₇B₈ magnets,” *Mater. Lett.*, vol. 5, no. 7, pp. 285–288, 1987.
- [4] H. Nakamura, K. Hirota, M. Shimao, T. Minowa, and M. Honshima, “Magnetic properties of extremely small Nd-Fe-B sintered magnets,” *IEEE Trans. Magn.*, vol. 41, no. 10, pp. 3844–3846, Oct. 2005.
- [5] R. Skomski and J. M. D. Coey, “Giant energy product in nanostructured two-phase magnets,” *Phys. Rev. B*, vol. 48, no. 21, pp. 15812–15816, Dec. 1993.
- [6] R. Skomski, “Aligned two-phase magnets: Permanent magnetism of the future?,” *J. Appl. Phys.*, vol. 76, no. 10, pp. 7059–7064, 1994.
- [7] D. J. Sellmyer and R. Skomski, *Advanced magnetic nanostructures*. Springer, 2006.
- [8] T. Schrefl, H. Kronmüller, and J. Fidler, “Exchange hardening in nano-structured two-phase permanent magnets,” *J. Magn. Magn. Mater.*, vol. 127, no. 3, pp. L273–L277, Oct. 1993.
- [9] S. Bance, H. Oezelt, T. Schrefl, G. Ciuta, N. M. Dempsey, D. Givord, M. Winklhofer, G. Hrkac, G. Zimanyi, O. Gutfleisch, T. G. Woodcock, T. Shoji, M. Yano, A. Kato, and A. Manabe, “Influence of defect thickness on the angular dependence of coercivity in rare-earth permanent magnets,” *Appl. Phys. Lett.*, vol. 104, no. 18, p. 182408, May 2014.
- [10] G. Hrkac, T. G. Woodcock, C. Freeman, A. Goncharov, J. Dean, T. Schrefl, and O. Gutfleisch, “The role of local anisotropy profiles at grain boundaries on the coercivity of Nd₂Fe₁₄B magnets,” *Appl. Phys. Lett.*, vol. 97, no. 23, p. 232511, 2010.
- [11] H. Sepehri-Amin, T. Ohkubo, and K. Hono, “Grain boundary structure and chemistry of Dy-diffusion processed Nd-Fe-B sintered magnets,” *J. Appl. Phys.*, vol. 107, no. 9, p. 09A745, May 2010.
- [12] L. Exl, S. Bance, F. Reichel, T. Schrefl, H. P. Stimming, and N. J. Mauser, “LaBonte’s method revisited: An effective steepest descent method for micromagnetic energy minimization,” *J. Appl. Phys.*, vol. 115, no. 17, p. 17D118, May 2014.
- [13] T. Schrefl, G. Hrkac, S. Bance, D. Suess, O. Ertl, and J. Fidler, “Numerical Methods in Micromagnetics (Finite Element Method),” in *Handbook of Magnetism and Advanced Magnetic Materials*, John Wiley & Sons, Ltd, 2007.
- [14] W. Rave, K. Ramstöck, and A. Hubert, “Corners and nucleation in micromagnetics,” *J. Magn. Magn. Mater.*, vol. 183, no. 3, pp. 329–333, Mar. 1998.
- [15] K.-D. Durst and H. Kronmüller, “Determination of intrinsic magnetic material parameters of Nd₂Fe₁₄B from magnetic measurements of sintered Nd₁₅Fe₇₇B₈ magnets,” *J. Magn. Magn. Mater.*, vol. 59, no. 1, pp. 86–94, 1986.
- [16] M. Sagawa, S. Hirosawa, K. Tokuhara, H. Yamamoto, S. Fujimura, Y. Tsubokawa, and R. Shimizu, “Dependence of coercivity on the anisotropy field in the Nd₂Fe₁₄B-type sintered magnets,” *J. Appl. Phys.*, vol. 61, no. 8, pp. 3559–3561, 1987.
- [17] M. J. Hawton, “An investigation of anisotropic magnetic properties of bare barth iron boron alloys,” Durham University, 1943.
- [18] M. E. Schabes and H. N. Bertram, “Magnetization processes in ferromagnetic cubes,” *J. Appl. Phys.*, vol. 64, no. 3, p. 1347, 1988.
- [19] C. Serpico, I. D. Mayergoyz, and G. Bertotti, “Numerical technique for integration of the Landau–Lifshitz equation,” *J. Appl. Phys.*, vol. 89, no. 11, pp. 6991–6993, 2001.
- [20] I. Loris, M. Bertero, C. De Mol, R. Zanella, and L. Zanni, “Accelerating gradient projection methods for -constrained signal recovery by steplength selection rules,” *Appl. Comput. Harmon. Anal.*, vol. 27, no. 2, pp. 247–254, Sep. 2009.
- [21] E. Weinan, W. Ren, and E. Vanden-Eijnden, “Simplified and improved string method for computing the minimum energy paths in barrier-crossing events,” *J. Chem. Phys.*, vol. 126, no. 16, p. 164103, 2007.
- [22] P. Gaunt, “Magnetic viscosity and thermal activation energy,” *J. Appl. Phys.*, vol. 59, no. 12, p. 4129, 1986.

- [23] D. Givord, P. Tenaud, and T. Viadieu, "Angular dependence of coercivity in sintered magnets," *J. Magn. Magn. Mater.*, vol. 72, no. 3, pp. 247–252, 1988.
- [24] D. Givord, Q. Lu, M. F. Rossignol, P. Tenaud, and T. Viadieu, "Experimental approach to coercivity analysis in hard magnetic materials," *J. Magn. Magn. Mater.*, vol. 83, no. 1, pp. 183–188, 1990.
- [25] D. Givord, M. Rossignol, and V. M. Barthem, "The physics of coercivity," *J. Magn. Magn. Mater.*, vol. 258, pp. 1–5, 2003.
- [26] P. Gaunt and G. J. Roy, "Magnetic viscosity in ferromagnets: II. Co₅Ce permanent magnet particles," *Philos. Mag.*, vol. 34, no. 5, pp. 781–788, Nov. 1976.